

# Concepts and Preliminary Data Toward the Realization of Image-guided Liver Surgery

David M. Cash · Michael I. Miga · Sean C. Glasgow ·  
Benoit M. Dawant · Logan W. Clements · Zhujiang Cao ·  
Robert L. Galloway · William C. Chapman

Published online: 26 April 2007

© 2007 The Society for Surgery of the Alimentary Tract

**Abstract** Image-guided surgery provides navigational assistance to the surgeon by displaying the surgical probe position on a set of preoperative tomograms in real time. In this study, the feasibility of implementing image-guided surgery concepts into liver surgery was examined during eight hepatic resection procedures. Preoperative tomographic image data were acquired and processed. Accompanying intraoperative data on liver shape and position were obtained through optically tracked probes and laser range scanning technology. The preoperative and intraoperative representations of the liver surface were aligned using the iterative closest point surface matching algorithm. Surface registrations resulted in mean residual errors from 2 to 6 mm, with errors of target surface regions being below a stated goal of 1 cm. Issues affecting registration accuracy include liver motion due to respiration, the quality of the intraoperative surface data, and intraoperative organ deformation. Respiratory motion was quantified during the procedures as cyclical, primarily along the cranial–caudal direction. The resulting registrations were more robust and accurate when using laser range scanning to rapidly acquire thousands of points on the liver surface and when capturing unique geometric regions on the liver surface, such as the inferior edge. Finally, finite element models recovered much of the observed intraoperative deformation, further decreasing errors in the registration. Image-guided liver surgery has shown the potential to provide surgeons with important navigation aids that could increase the accuracy of targeting lesions and the number of patients eligible for surgical resection.

**Keywords** Image-guided surgery · Liver resection · Surface registration · Laser range scanning · Finite element

Of the 147,000 projected new cases of colorectal cancer for 2004,<sup>1</sup> it is estimated that 50% of all colorectal primary tumors will develop a liver metastasis at some point in the disease, and 20% of cases will develop a metastasis solely

in the liver.<sup>2</sup> Metastatic liver cancer takes a rapid course. When untreated, the median survival rate is between 5 and 12 months with a 5-year survival rate approaching zero.<sup>3–6</sup> The most common form of treatment is surgical resection. For metastases, studies have reported a 5-year survival rates of 20–50%, with much of the variance attributed to bias in patient selection. For primary liver tumors, the 5-year

---

This work was presented at the annual meeting of the American Hepato-Pancreatobiliary Association, April 14–17, 2005, Fort Lauderdale, Florida.

---

D. M. Cash · M. I. Miga · L. W. Clements · Z. Cao ·  
R. L. Galloway  
Department of Biomedical Engineering, Vanderbilt University,  
Nashville, TN, USA

D. M. Cash · S. C. Glasgow · W. C. Chapman  
Department of Surgery,  
Washington University School of Medicine,  
Nashville, TN, USA

D. M. Cash · R. L. Galloway  
Pathfinder Therapeutics, Inc., Nashville, TN, USA

B. M. Dawant · Z. Cao · W. C. Chapman  
Department of Electrical Engineering and Computer Science,  
Vanderbilt University,  
Nashville, TN, USA

W. C. Chapman (✉)  
Department of Surgery,  
Washington University School of Medicine,  
660 S. Euclid Ave., Box 8109, St. Louis, MO 60301, USA  
e-mail: chapman@wustl.edu

survival rates varied from 24 to 76% due to variables such as age, size of tumor, and presence of cirrhosis.<sup>2,7–10</sup> With 70–90% of all patients ineligible for resection, ablative techniques provide a promising alternative.<sup>11–15</sup>

In the cases of resection and ablation, if the surgeon can direct therapy to the target with an ever higher degree of accuracy, it could lead to smaller resection margins, improved outcomes, and more patients eligible for treatment. To that end, image-guided surgical techniques could provide this improvement in accuracy over conventional techniques. At the heart of image-guided surgery (IGS) is a process known as registration in which a mathematical mapping is determined between the intraoperative anatomical presentation of the organ and the preoperatively acquired tomograms. From this mapping, a real-time update of surgical position can be displayed in reference to preoperative imaging studies. If intraoperative data are properly and accurately acquired for the liver, then a successful registration will provide navigational assistance to resect subsurface targets (tumors and cysts) and to avoid critical structures (vasculature and biliary trees), thus augmenting the anatomical expertise of the surgeon with an additional source of information. Image-guided surgery techniques are also quite flexible, as they can readily incorporate streams of data commonly available in the operating room, such as intraoperative ultrasound or physiological monitoring, and merge them with new modalities, such as the tracking and laser range scanning systems mentioned below.

Before computing a registration between image and physical space, translational motion due to respiration must be quantified and compensated. Many imaging studies of the liver have shown this motion to be periodic, principally in the cranial–caudal direction. A comprehensive review on the issue can be found.<sup>16</sup> Most studies report the magnitude of the motion to be on the order of 10–30 mm in the closed abdomen.<sup>17–20</sup> Herline et al.<sup>21</sup> acquired respiratory motion data during two open liver resection cases at three different locations on the liver surface. The motion also was observed to be periodic, and the mean ( $\pm$ SEM) distance between peak inhalation and peak exhalation was  $10.3 \pm 2.5$  mm. Banovac and Cleary<sup>22</sup> took results from prior studies on liver respiration and used them to develop a respiring liver phantom on which they performed needle placement experiments. In that study, two users were able to successfully puncture liver tumors in 87.5% of the attempts.

Previous registration studies involving image-guided liver surgery can be divided into three categories. The first set consists of registrations based on the geometric features of the liver. Corresponding features between the dataset are identified and aligned by minimizing a distance measure between the two sets of features.<sup>23–26</sup> The second category uses the complex, feature-rich liver vasculature to drive the

registration between preoperative images and intraoperative ultrasound data.<sup>27–29</sup> The final type of registration is intensity based, where a correlation measure between two image sets is maximized. This method requires intraoperative ultrasound or tomographic data and is intended for guidance during minimally invasive ablation applications.<sup>30–32</sup> Currently, most image-guided studies in the liver have been restricted to phantoms, animal models, and minimally invasive interventional cases. In this paper, we present the first description of surface registration using a laser range scanner during open abdominal hepatic tumor resections. Issues that could affect the accuracy of the registration, including liver motion due to respiration, were addressed and analyzed.

## Materials and Methods

### Image Acquisition and Segmentation

Preoperative image volumes were acquired by computed tomography (CT) or magnetic resonance imaging. Both modalities used triphase studies that produce an uncontrasted image volume, a volume with arterial phase contrast, and a third volume where the contrast has washed out of the arteries and provides more emphasis on the venous vasculature. This imaging protocol is standard for patients undergoing liver tumor resection. The pixel spacing for these images ranged from 0.6 to 1.0 mm. The preferred slice thickness was 2.0 mm although, in these studies, the acquired volumes ranged from 0.8 to 5.0 mm. For this study, it is highly desirable that the tomographic slices do not overlap.

From the resulting tomograms, the liver was segmented from the surrounding abdominal viscera. Two methods of segmentation were performed. The first involved the authors manually outlining the contour of the liver, which can take 4 h or longer. To greatly reduce user interaction, our group has developed a semiautomatic method<sup>33,34</sup> that is based on the level-set technique.<sup>35</sup> This method was specifically designed to identify the edges of the liver, which can be difficult to discern near the ribs and heart. After segmentation is completed, there is a brief review and user interaction phase with the surgeon to further refine the segmentation. Corresponding results from an example manual and semiautomatic segmentation of a CT slice are shown in Fig. 1. The segmented contours are used to generate a three-dimensional surface model using the marching cubes methods.<sup>36</sup> Further refinement is performed using surface fitting software (FastRBF Toolkit; FarField Technology, Christchurch, New Zealand) involving radial basis functions as described previously.<sup>37</sup> This method provides a smoother representation with less points as illustrated in Fig. 2.

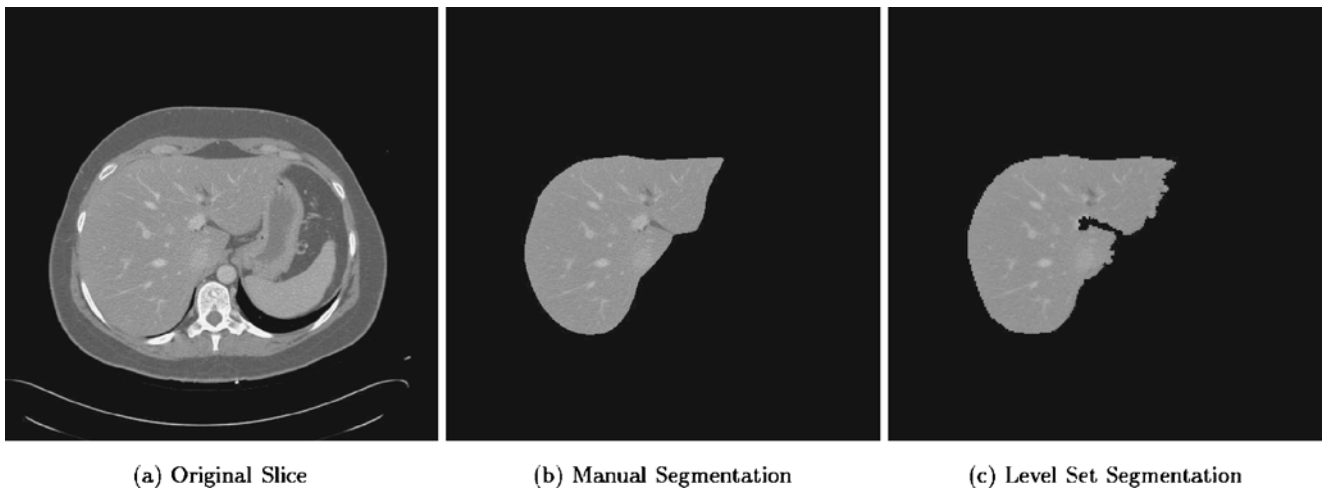


**Figure 1** Comparison of manual and level-set segmentations of the liver.

### Intraoperative Data

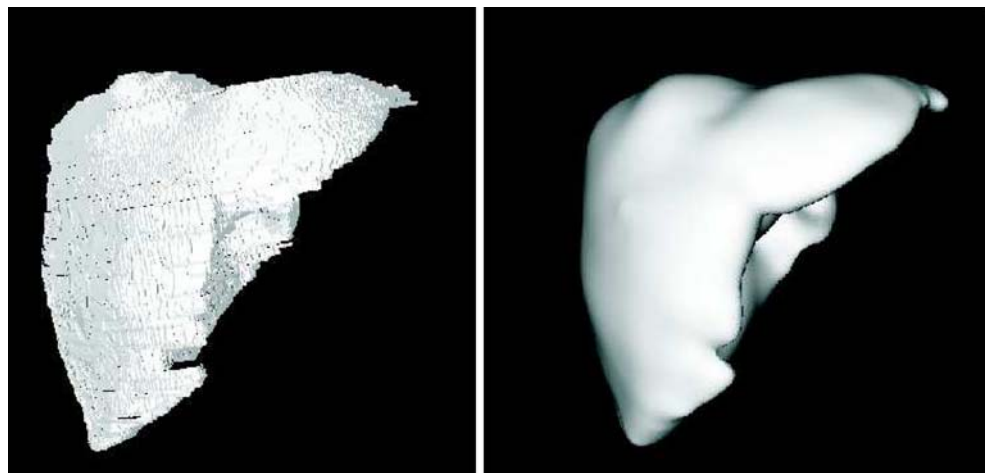
To digitize individual points in three-dimensional space, the OPTOTRAK 3020 (Northern Digital, Waterloo, Ontario, Canada) optical localization system was used. The system consists of an infrared camera, which determines the position and orientation of specialized probes embedded with infrared diodes (IREDs). Points are digitized by placing them in contact with the probe tip. The OPTOTRAK system is capable of acquiring single points with a root-mean-square accuracy of 0.1 mm.<sup>38</sup> Surface data are generated by sweeping the probe across the entire organ, allowing the tracking system to rapidly collect digitized points on the surface. For this study, the update rate for the probe's position was set to 40 Hz. Figure 3 displays the OPTOTRAK system in use, acquiring points on the liver surface.

Dense surface representations were acquired intraoperatively with a commercially available laser range scanner (RealScan 200C; 3D Digital Corp., Sandy Hook, CT, USA). This method serves as a complementary means to

acquire surface data. The range scanner uses the principle of optical triangulation to rapidly capture thousands of three-dimensional points in a noncontact fashion. The laser used is very low in power, a class I eye-safe laser, and orders of magnitude below the maximum permissible exposure level for skin as stated in the American National Standard for Safe Use of Lasers (ANSI Z136.1). The range scanner itself is relatively compact (9.6×9.8×3.1 inches), as can be seen in Fig. 3, where it has been positioned in the operating room. Ongoing research is being performed in collaboration with the authors to develop a laparoscopic range scanner that will allow for dense surface acquisition in minimally invasive procedures.<sup>39</sup>

In addition to collecting three-dimensional surface data, the scanner simultaneously acquires a video image of the scene and then texture maps the appropriate color information onto each three-dimensional point. The texture-mapped point data are extremely useful in identifying the exposed liver surface from the resulting range scans and in segmenting it from the rest of the intraoperative scene. Figure 4 shows the video image acquired by the scanner,

**Figure 2** Surface model generation from the segmented contours. The initial surface mesh (*left*) is generated using the marching cubes method. It is refined (*right*) with a surface fitting technique that employs radial basis functions,<sup>37</sup> providing a smoother surface with less vertices, potentially increasing the speed and accuracy of the registration.



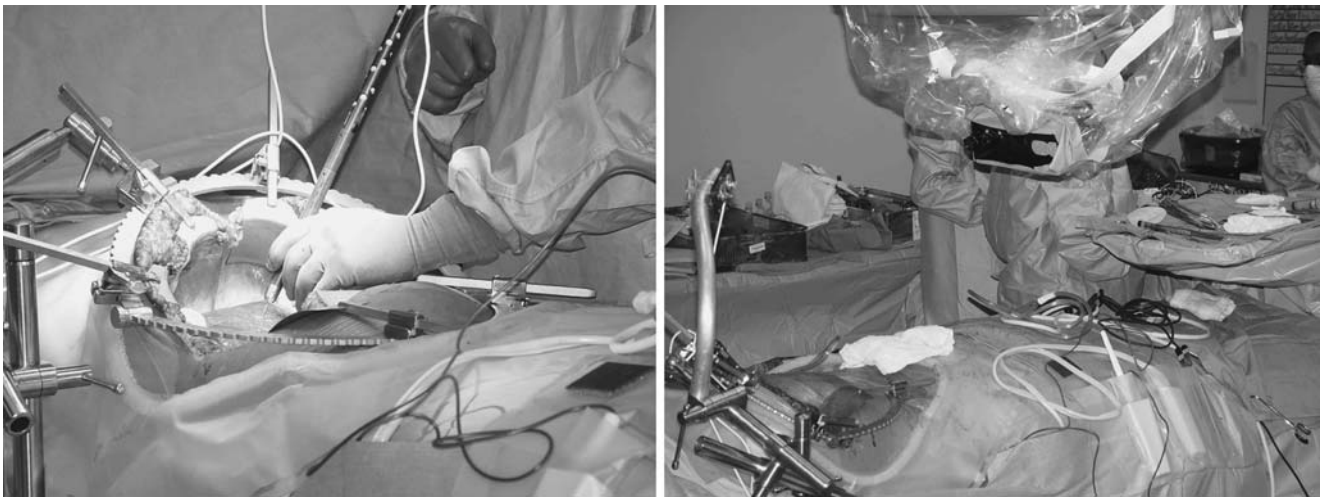


**Figure 3** Surface data acquisition in the operating room. In the *left image*, the surgeon is digitizing points on the liver surface with the optically tracked probe. The *right image* shows the range scanner in position to acquire surface data of the liver intraoperatively.

along with the three-dimensional point cloud and how these data sets are combined with texture mapping.

To have relevance in the surgical suite, the output points of the range scanner must be reported in reference to the OPTOTRAK localization system. To that end, individual IREDs that are tracked by the OPTOTRAK camera are

rigidly attached to the scanner. A calibration procedure was developed to link the position of the IREDs with the range scanner system, and tracking studies were performed.<sup>26–40</sup> A more robust method of IRED placement on the range scanner was developed, allowing for tracking with sub-millimetric errors.<sup>41</sup>

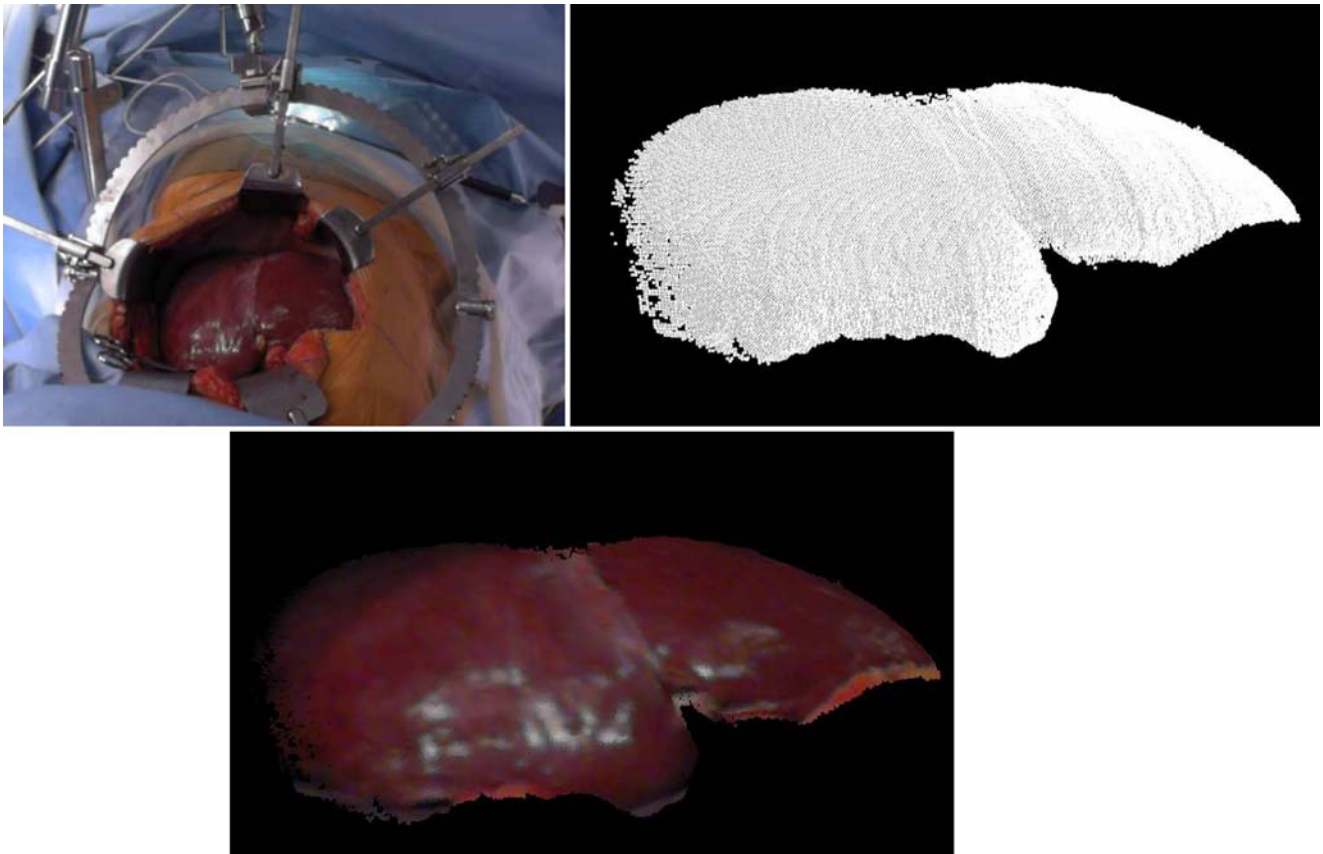


**Figure 4** Data acquisition with the range scanner. The video snapshot on the *top left* and the three-dimensional data on the *top right* are combined to form a texture mapped point cloud, which is shown in the *bottom image*.

## Rigid Registration

The surface of the liver has been chosen as the feature for registration. Intraoperative surface data are acquired using the range scanner or the tracked probe. These data are then registered with the surface model generated from the preoperative tomographic image volume using the iterative closest point (ICP) method.<sup>42</sup> To make the searching process more efficient, *k*-*d* trees were used.<sup>43,44</sup>

The ICP registration method can be susceptible to gross misalignment if a suitable initial estimate is not provided. We identify anatomical landmarks on or near the liver and use them to obtain an initial registration. Before the procedure, a set of four or five landmarks is identified in the image volume by the surgeon, and the landmarks' three-dimensional image coordinates are recorded. Typical landmarks include the inferior tip of the liver, the lateral tip of the right lobe, the portal vein bifurcation, and the junction of the inferior vena cava with the liver. In some instances, unique geometric features on the exposed liver surface are used. Then, the corresponding positions of these landmarks are identified intraoperatively by touching them with the tracked probe and recording the probe's position. Once the position of each anatomical landmark has been acquired, a point-based registration is computed that minimizes the root-mean-square distance between corresponding anatomical landmarks.<sup>45–47</sup> Due to the possibility of deformation and the difficulty in localizing landmarks, the resulting transformation is not accurate enough for guidance, but it usually can provide an acceptable guess that is close enough to result in ICP reaching a suitable minimum.

## Intraoperative Deformation

The liver consists of soft tissue that undergoes deformation due to a number of surgical loads (resection, immobilization, and repositioning). Deformation could compromise the accuracy of targeting lesions if only a rigid mapping is used to register between the intraoperative data and the preoperative images. Thus, we implemented a biomechanical model of the liver using the finite element method (FEM) to handle deformation. The FEM analysis provides a powerful tool for modeling soft-tissue deformation and has been applied to the brain shift problem in neurosurgical procedures.<sup>48–51</sup> Efforts to implement finite element modeling in liver resections have been limited to virtual reality and surgical simulation, where accuracy of the deformation is sacrificed to achieve realistic deformations at real-time frame rates for the purposes of training and planning.<sup>52–55</sup> To begin the analysis, a volumetric mesh is generated from the patient's preoperative images, and it serves as the model used to solve a system of partial differential equations, which simulates the patient's liver undergoing a deforma-

tion. The simulation is driven by boundary conditions that describe the forces interacting with the liver surface. Some regions of the liver are held fixed, whereas others move freely. The third and most important category of boundary condition deforms points on the liver surface to match them with the intraoperative representation. More information on the implementation of the finite element model can be found in Cash et al.<sup>56</sup>

## Surgical Navigation Software

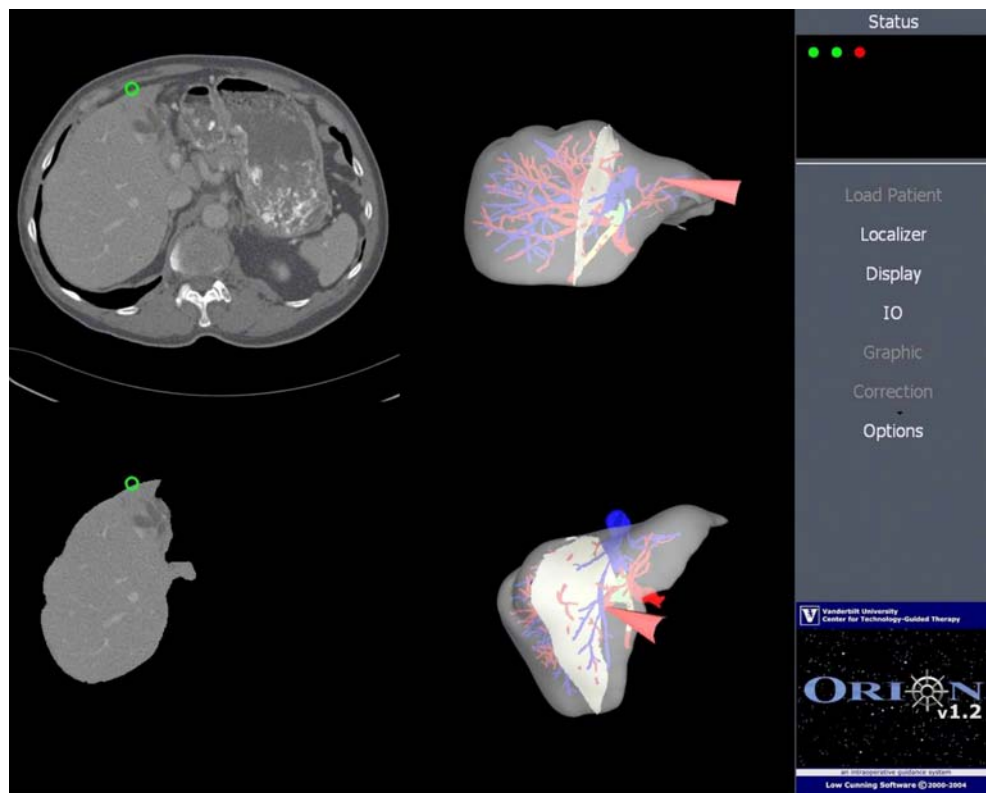
The Operating Room Image-Oriented Navigation (ORION) system was created at Vanderbilt University to handle the tasks required for an image-guided surgical procedure. ORION was developed under Windows NT/2000 using Microsoft Visual C++ 6.0 and Win 32 API. Under the current framework, ORION is capable of rendering updates at a rate of 30–40 frames per second. For this study, new components were developed in ORION that involved fast surface registration, communication with the laser range scanner, and three-dimensional rendering of the liver surface. In addition, our group has collaborated with MeVis (Center for Medical Diagnostic Systems and Visualization, Bremen, Germany) to incorporate their vascular segmentation and representation capabilities<sup>57</sup> for surgical planning into ORION so that it can display the probe position with respect to their models of the vasculature, tumors, and resection planes. A screen shot from ORION during one of the procedures is shown in Fig. 5.

## Clinical Acquisition

Institutional review board approval was obtained at both Vanderbilt University Medical Center and Washington University School of Medicine for the intraoperative acquisition of liver surface data. Informed consent was obtained from eight patients (five at Vanderbilt and three at Washington University) undergoing standard liver tumor resection procedures. Of these eight cases, only one patient was undergoing resection for a primary tumor; the other seven presented with metastatic liver tumors. Three of the patients were female, whereas five of the patients were male, and their mean age was  $59.4 \pm 9.2$  years. The results presented from case 6 of this group have been previously published by our group.<sup>26,58</sup>

For the purpose of registration, planned periods of apnea were used to decrease respiratory-related liver motion. These apneic periods were part of the approved institutional review board protocol, and each occurred at the same point in the respiratory cycle so that the liver would reside approximately in the same location for every registration. There were two to five brief apneic periods, each lasting no more than 4 min, over the course of the procedure. During

**Figure 5** Screen shot of the ORION surgical navigation software. ORION is displaying, from the *top-left panel clockwise*, the native tomogram, two different perspectives of the three-dimensional liver and the vasculature as segmented by MeVis, and a tomographic slice of the segmented liver.



each apneic period, physical space data were acquired for the registration process. First, point-based landmarks were digitized with a sterilized, tracked probe for the purposes of determining an initial estimate of the registration that served as input to the ICP algorithm. After the initial alignment, surface data were captured with either the probe or the range scanner. The probe was placed in contact with the liver and swept across the surface. The range scanner attaches to a surgical arm that stays out of the operating field while not in use. When ready to scan, the surgical arm is swiveled into the intraoperative scene as shown in Fig. 3. After a brief setup for positioning the scanner and determining the correct parameters, the surface is scanned. The scanner has the potential to acquire anywhere from 15,000 to 45,000 points on the liver surface. The number of points acquired is dependent on the organ size and the area of liver surface visible to the scanner. In four of the eight cases, range scan data of the liver surface were available. In all but one case, surface data were acquired using an optically tracked probe.

**Experimental Studies**

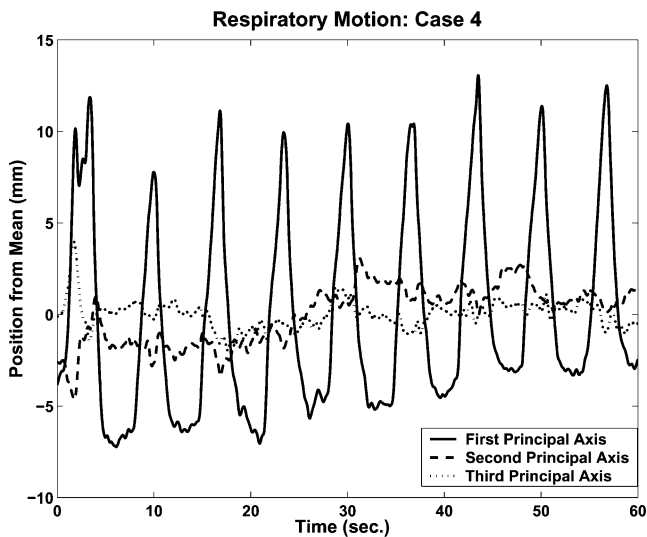
In this study, three separate experiments were performed in the operating room to determine the feasibility of this image-guided liver surgery system. The first set of experiments examined the nature and magnitude of motion in the liver due to respiration. In these experiments, a tracked probe was

placed on the liver surface, and three-dimensional position information was acquired for 30–60 seconds, corresponding to 4–10 breathing cycles. During this acquisition, the tip of the probe was placed on a point of the liver surface. The surgeon maintained contact with this point and allowed the probe to move with the organ during the respiratory cycle. The probe tip’s three-dimensional position was recorded at a rate of 40 Hz, and the time course of this position data represented the motion path for this particular liver surface point during respiration. To analyze the resulting motion data, noise was removed using a moving average filter. Then, the three-dimensional path representing the liver point’s motion during these respiratory cycles was examined using principal

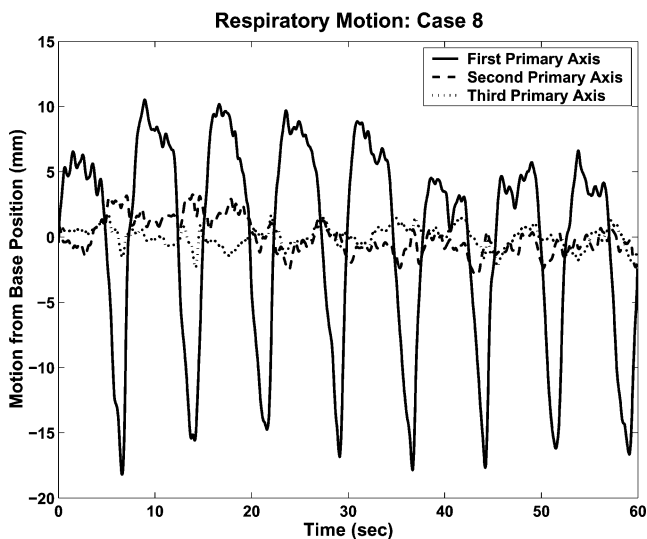
**Table 1** Principle Component Analysis of Respiratory Motion Data

Case	Percent of motion attributed to primary axis	Motion along primary axis (mean±SEM) (mm)
1	87	12.5±1.2 (n = 5)
3	97	11.2±3.5 (n = 4)
4	91	17.1±1.4 (n = 21)
5	74	6.8±1.8 (n = 13)
6	80	14.1±1.7 (n = 7)
7	80	11.9±2.0 (n = 6)
8a	96	24.6±1.9 (n = 8)
8b	98	29.7±1.2 (n = 8)

No respiratory data were acquired in case 2, and two separate sets of respiratory data were acquired in case 8.



(a) Case 4



(b) Case 8

**Figure 6** Time plot of respiratory data. The data are aligned according to the axes provided by the primary component analysis. The origin is the mean of the original respiration data.

component analysis (PCA). This PCA reorganizes the coordinate system so that it is aligned with the three axes where the variance is the greatest. If PCA indicates that the variance along one of these axes is greater than the other two, this signifies that the point travels primarily along one dimension during respiration.

The second set of experiments focused on the accuracy of the surface registration algorithm. For each subject, two registrations were performed. “Registration A” involved computing the registration between the intraoperative surface data of the patient and the preoperative surface manually

**Table 2** Surface Registrations Between Intraoperative Range Scan Data and Preoperative Surfaces

Case	No. of scan points	Registration A (manual) RMS residual (mm)	Registration B (semiautomatic) RMS residual (mm)	RMS difference (A to B) (mm)
1	19,000	6.2 (18.7)	6.4 (19.8)	1.8 (3.2)
2	20,000	5.0 (18.4)	5.0 (16.7)	2.2 (3.3)
6	29,000	2.3 (11.9)	2.3 (11.5)	1.4 (2.7)
7	48,000	5.5 (19.2)	5.2 (18.5)	3.5 (5.7)

Registration A involves manually segmented preoperative surfaces. Registration B uses surfaces from the semiautomatic level-set technique. The second column indicates the number of intraoperative data points (rounded to the nearest 1,000). The third and fourth columns provide the root-mean-square (RMS) (and maximum) surface residual for registrations A and B. The final column holds the RMS difference between registrations A and B.

segmented from the tomographic data. “Registration B” performed the same registration except that it used the results from the level-set semiautomatic segmentation rather than the manual method. Both registrations used the same intraoperative data and transformed them into the preoperative image coordinate system. The difference between these registrations was defined by taking each point in the intraoperative surface and calculating the distance between its resulting position from registration A and its resulting position from registration B. If the root-mean-square distance taken over all the intraoperative points is small, it indicates that the two registrations produce similar results. Similar registrations indicate that variations between the two segmentations are effectively negligible and the semiauto-

**Table 3** Surface Registrations Between Intraoperative Tracked Probe Data and Preoperative Surfaces

Case	No. of scan points	Registration A (manual) RMS residual (mm)	Registration B (semiautomatic) RMS residual (mm)	RMS difference (A to B) (mm)
2	1,600	6.5 (24.9)	6.7 (23.4)	2.3 (5.2)
3	500	5.7 (20.9)	5.0 (19.4)	19.5 (35.6)
4	1,500	5.0 (14.6)	4.9 (19.8)	5.6 (7.7)
5	700	6.0 (17.1)	5.9 (17.1)	6.5 (10.0)
6	2,400	3.0 (20.0)	3.0 (21.2)	1.2 (1.9)
7	1,900	6.4 (24.8)	6.4 (26.4)	2.9 (5.5)
8	2,200	6.5 (20.5)	6.0 (17.9)	3.7 (5.5)

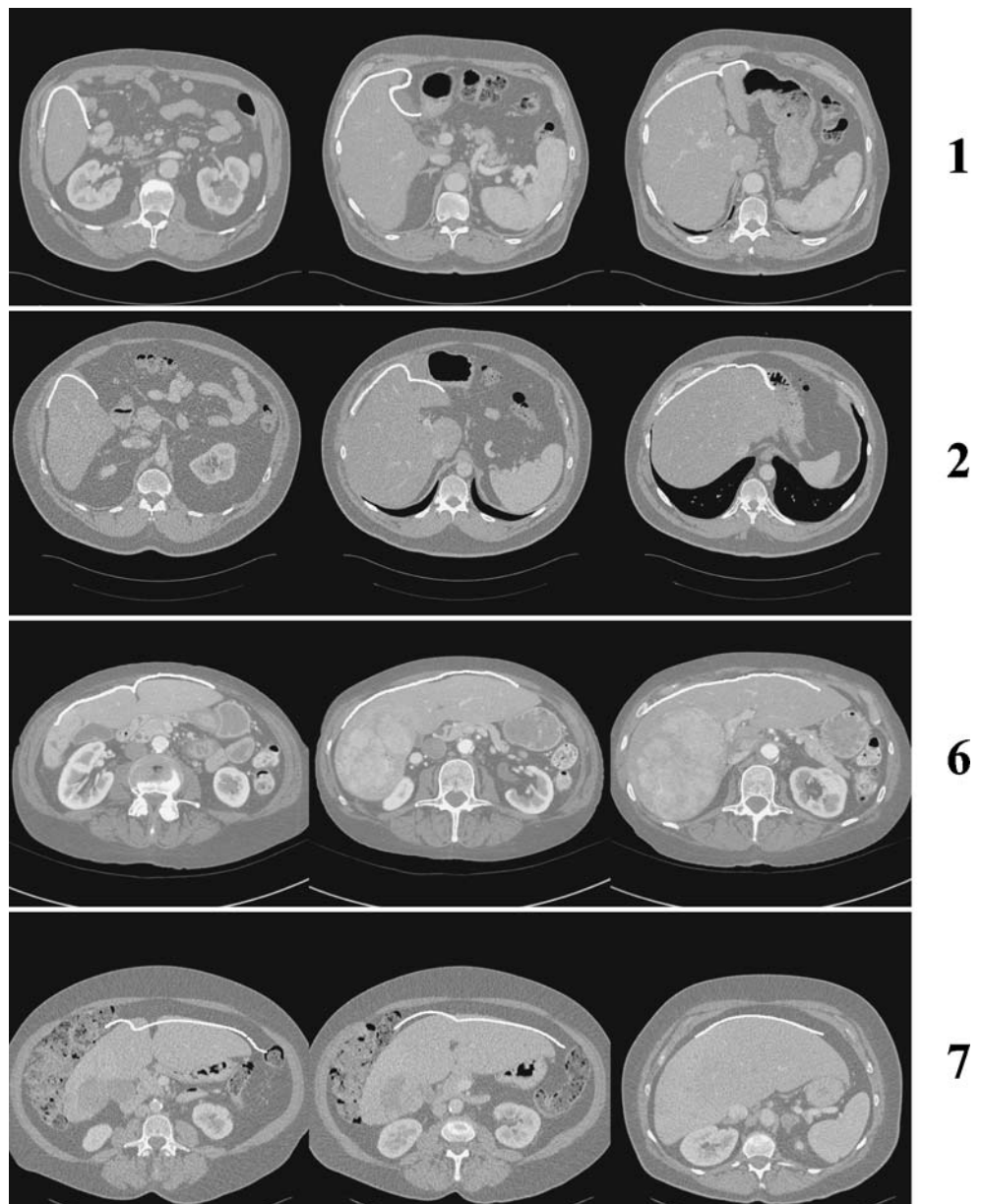
Registration A involves manually segmented preoperative surfaces. Registration B uses surfaces from the semiautomatic level-set technique. The second column indicates the number of intraoperative data points (rounded to nearest 1,000). The third and fourth columns provide the root-mean-square (RMS) (and maximum) surface residual for registrations A and B. The final column holds the RMS difference between registrations A and B.

matic segmentation will be suitable, thus greatly reducing processing time before surgery. Also, this result likely means that there are unique geometric features that were captured both intraoperatively and preoperatively, which drive the rigid registration to the same end result.

To assess the accuracy of the registration, targeting studies were performed as part of the registration experiments. Targets are geometrical features that can be identified in both the intraoperative and preoperative data but are not involved as part of the registration process. The most reliable targets are point-based landmarks that can be localized in both modalities with a high degree of accuracy. However, there are no point-based rigid landmarks available during this application, so other methods of targeting

must be developed. For three of the cases, the inferior edge of the liver could be manually identified in the range scan data, and it was broken into three adjoining regions to serve as targets for initial studies. When one of these regions served as the target region, it was removed from both surfaces. After the registration was performed, a surface target error was calculated. Two metrics were used for surface target error. The first was a root-mean-square closest-point residual error between the two targets, identical to the metric used in the registration algorithm itself. A more rigorous metric uses the distance between each point on the preoperative target region and the intersection where the point's surface normal crosses with the intraoperative target surface.

**Figure 7** Iterative closest point registration results. For each case, the registered range scan data is overlaid on top of the three tomographic slices from the volume.





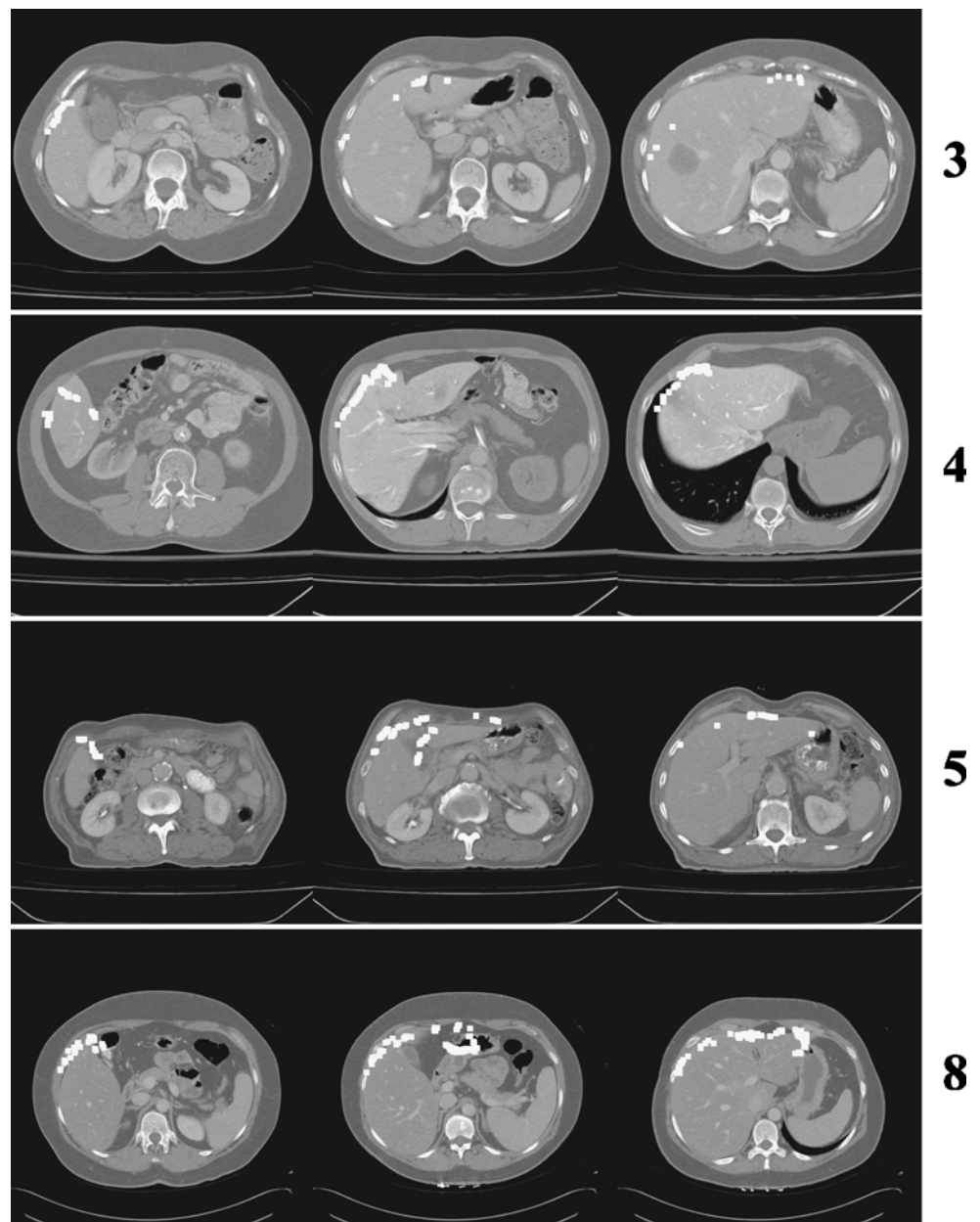
The final set of experiments tested the ability of the finite element model to compensate for intraoperative deformation remaining after the rigid alignment. First, a tetrahedral mesh was constructed based on segmentations of the preoperative data. Then, boundary conditions were applied to the model that represented the intraoperative conditions, fixing immobilized parts of the liver and forcing displacements in other regions that were dictated by their distance to the rigidly registered intraoperative data. Once the boundary conditions were applied, the displacements were solved using the FEM model. The resulting deformed mesh was overlaid on top of the preoperative tomograms and intraoperative data to qualitatively assess the results.

## Results

### Respiratory Motion

Table 1 shows the results from the PCA of respiratory motion. No respiratory data are available for case 2. Two sets of data from different time points during surgery were available for case 8. For each case, the percentage of motion that is attributed to the primary axis is shown, along with the average motion in millimeters between peak inhalation and peak exhalation that the liver moves along the primary axis. Figure 6 shows time plots of respiratory data from cases 4 and 8. The three plots represent each of

**Figure 8** Iterative closest point registration results. For each case, the registered probe data are overlaid on top of the three tomographic slices from the volume.



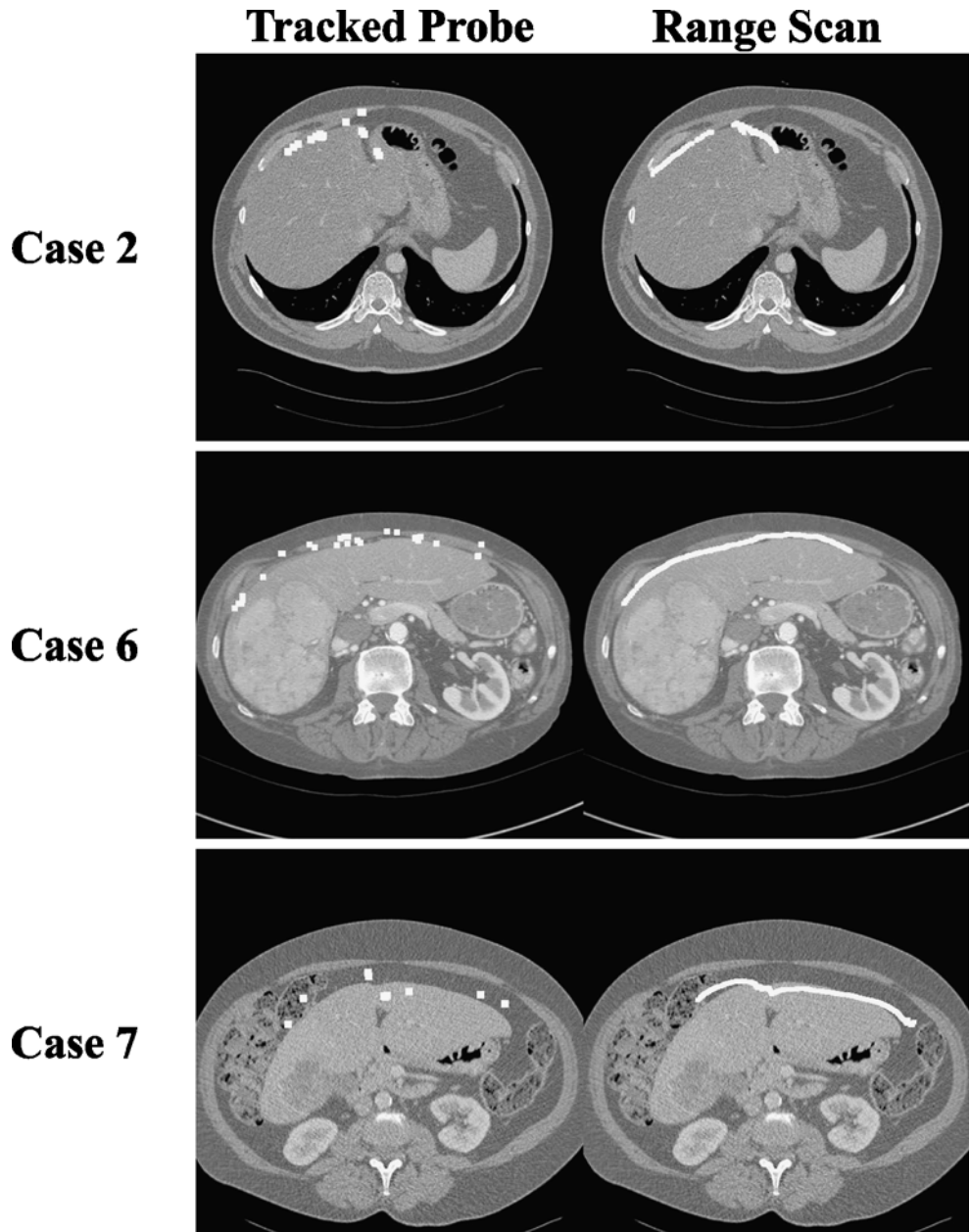
the three primary axes as determined by PCA. The origin represents the mean position of this data.

**Surface Registration**

The segmented surfaces used for registration studies contained 45,000 to 80,000 vertices. However, for each individual subject, the difference between manual and level-set segmented surfaces was not greater than 3,000 vertices. Table 2 shows the results from registrations between intraoperative range scan data and preoperative tomograms, whereas Table 3 shows the results from the registrations between tracked probe data and the preoper-

ative tomograms. In these tables, the second column indicates the number of intraoperative surface points acquired, which was rounded to the nearest 100. The values in the third and fourth columns represent the root-mean-square surface residual error (with the maximum closest point distance given in parentheses) for registrations based on the manual (registration A) and semiautomatic (registration B) segmented surfaces. This root-mean-square residual is the metric used in the minimization process of the ICP algorithm and describes the total error of fit between the two surfaces. However, sometimes, this value may be misleading with regard to accuracy in the resulting registration. The final column is the measure of similarity

**Figure 9** Comparison of surface registrations using tracked probe (*left column*) and range scan (*right column*). Both data-sets are overlaid on the identical slice from the image volume.



between the registrations using these two surfaces. This measure is the root-mean-square distance that separates the resulting location of points transformed by registration A versus registration B.

Figures 7 (range scan data) and 8 (tracked probe data) show a graphical representation of the registration results. In these figures, the intraoperative data are overlaid onto the corresponding tomographic slices. In three cases, both tracked probe data and range scan data of the liver surface were available, and each modality was used for a surface registration. A comparison of the resulting registrations is shown in Fig. 9, where both datasets are overlaid on the same tomographic slice using the respective registrations.

The results of the targeting studies are found in Table 4. In each case, the inferior edge is broken into three regions (left, middle, and right), which serve as surface targets. The target regions were removed from the surfaces before registration and then used after the registration to compute two metrics: the standard root-mean-square closest point residual and the distance between points in the target surfaces along the normal vector. These two metrics are shown in the fourth and fifth columns, respectively.

#### Finite Element Modeling

Figure 10 shows the results from the patient model, where the displacements at each node have been used to warp the preoperative image. The deformed image is fused with the preoperative data and the registered point cloud to show the difference between the registration before and after implementation of the finite element model. The boundary conditions provide a good agreement between the deformed preoperative surface and the intraoperative surface data. The inside of the liver, where data are unavailable, is displaced in a manner that is determined by the underlying biomechanics of the finite element model.

#### Discussion

This study attempts to provide the framework for applying IGS concepts to liver resections. We show how this framework has been applied during initial clinical settings and analyze some of the most significant issues that could affect the surface registration. With a successful registration, the ORION system can provide powerful navigation aids to the surgeon as illustrated in Fig. 5. It can display the position of a tracked surgical instrument in relation to preoperative tomographic volumes and rendered surfaces, including important subsurface vasculature and tumors. This will allow the surgeon to have real-time quantitative information regarding the proximity of critical vascular and biliary structures as well as preoperative resection plans.

Providing navigation assistance to the surgeon using preoperative tomograms through IGS could provide some potential advantages over intraoperative ultrasound (IOUS) alone, which is the most common form of providing intraoperative navigation in liver surgery. First, accurate registration of nonvisible tumors to the operating-room environment would allow for maximum retention of healthy unaffected liver tissue by allowing tighter margins. Second, these nonrigid model-based deformation methods will not only improve tumor registration but also the underlying vascular network; that is, the methods will also allow for nonrigid alignment of computerized tomographic angiography, which is of primary importance in resective therapy. Finally, subsurface tumors can confound vascular representation in IOUS; if this method is performed in conjunction with coregistered IOUS, discrepancies in vascular ultrasound images may be corrected.

Other researchers have focused their efforts on phantom studies<sup>25,27</sup> and percutaneous studies,<sup>24,28,30–32</sup> but this work is unique in that it concentrates on acquiring and registering data from open abdominal hepatic tumor resections. Our initial work was also based on phantom studies, which resulted in registration errors of 2.9 mm and targeting errors of 2.8 mm.<sup>23</sup> The updated system, which was used for these studies, used the laser range scanner to reduce registration errors and target errors in phantom studies to under 0.8 and 2.0 mm, respectively.<sup>26</sup> The clinical findings result in higher registration errors due to the presence of a number of factors that can be eliminated during idealized phantom studies. The most important aspects are the decrease in the exposed surface region that can be acquired by the range scanner and the presence of

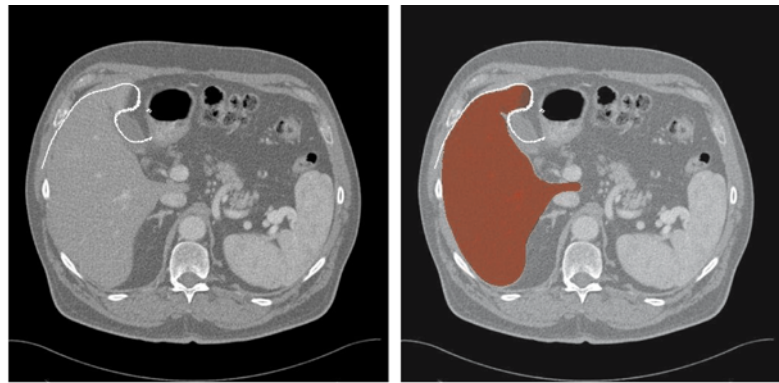
**Table 4** Results of Targeting Studies During Surface-based Rigid Registration

Case	Target	No. of points	Mean residual (mm)	Normal distance (mm)
1	Right	1,700	5.1±3.5	4.7±2.5
	Middle	1,500	5.1±3.5	5.6±2.7
	Left	2,700	4.8±3.5	9.3±3.7
2	Right	3,000	5.0±3.7	4.5±3.7
	Middle	1,900	4.9±3.6	7.9±4.5
	Left	1,500	4.9±3.7	9.0±5.1
7	Right	1,000	4.5±2.9	5.2±4.3
	Middle	1,600	4.4±2.9	5.5±5.2
	Left	1,300	4.5±3.0	2.6±2.5

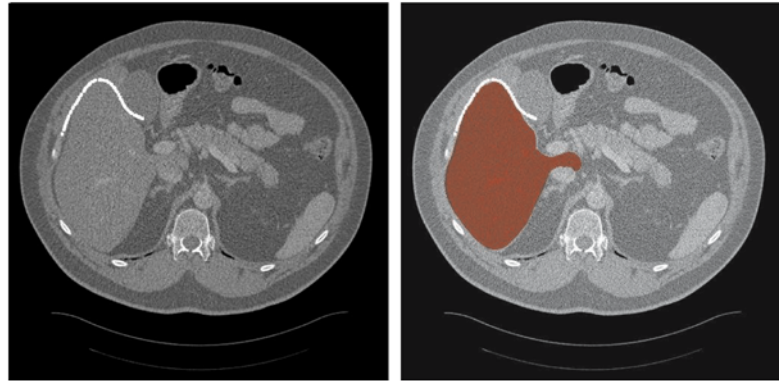
In these studies, the targets are based on the inferior ridge of the liver broken into three regions. There are two metrics listed for each target. The first metric is a closest point distance (mean±SEM) in millimeters, which is listed in the fourth column. The second is the root-mean-square (mean±SEM) distance from each point on the preoperative target surface to where its surface normal intersects with the intraoperative target surface.

**Figure 10** *Left column*—Original rigid registration of range scan data overlaid on tomograms. *Right column*—The deformed liver volume from the finite element model is overlaid in red. In the areas where the point cloud was used for the boundary conditions, there is improved agreement between the range scan surface and the deformed image surface.

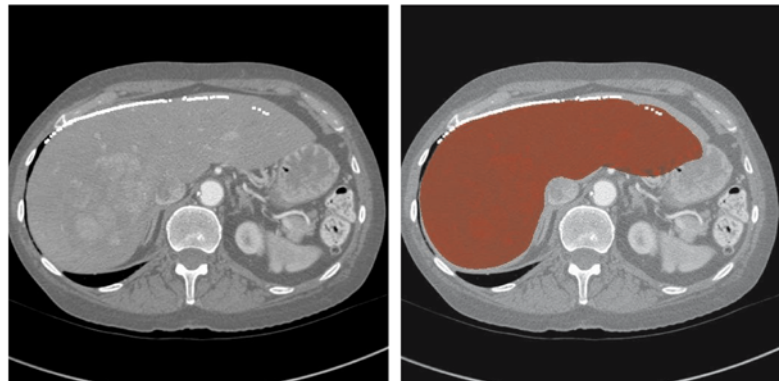
**Case 1**



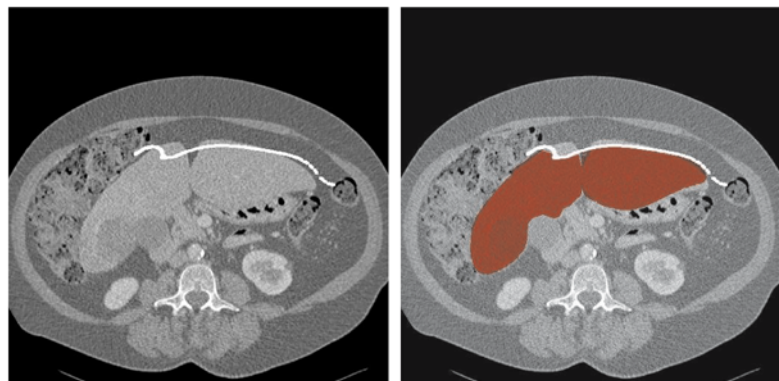
**Case 2**



**Case 6**



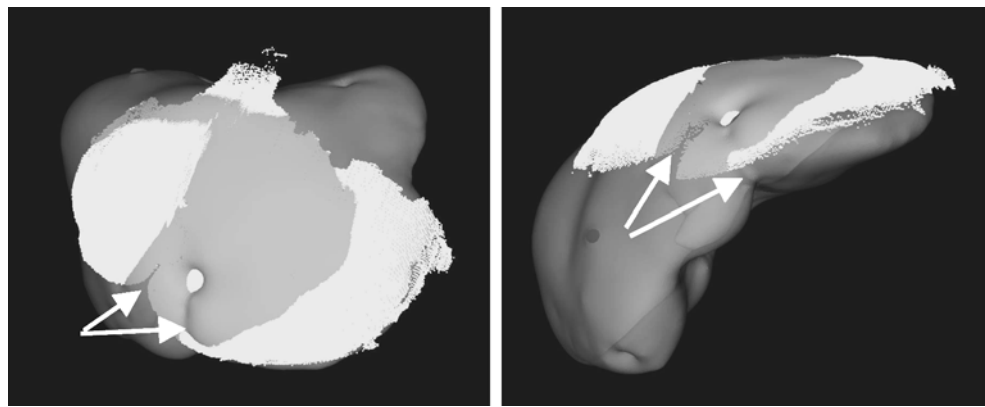
**Case 7**



intraoperative deformation. Other factors include the inaccuracies of the segmentation and the introduction of added noise to the range scan data caused by surrounding structures and surgical instruments located in the scanner’s field of view.

This study also examined the amount of respiratory motion in the liver observed during a procedure. Our group first examined respiratory motion when Herline et al.<sup>21</sup> did some initial studies in two human patients. His results indicated the mean  $\pm$  SEM motion of the liver during a

**Figure 11** In case 7, the relatively planar range scan data result in misalignments during the surface-based registration. The qualitatively identified landmark, where the falciform ligament resided before surgery, is rotated clockwise as indicated by the *white arrows*.



respiratory cycle was  $10.3 \pm 2.5$  mm. These results are consistent with the amplitude of respiratory motion in our findings. In addition, we used PCA to determine how much of the motion is along one dimension, as it has been done in related noninvasive imaging studies.<sup>17–20</sup> Their results indicate periodic one-dimensional motion along the cranial–caudal axis on the order of 10–30 mm. However, in our intraoperative data, there is some misalignment present when the primary axis of the motion is transformed into image space and compared to the imaging axis that corresponds to the cranial–caudal direction. This misalignment could be caused by registration errors or patient positioning on the imaging gantry, but another significant cause could be the repositioning of the liver during surgery. Thus, the intraoperative orientation with respect to the cranial–caudal axis has been modified. This information will be valuable for future studies to account for this motion and lower the number of apneic periods.

From Table 2, the range scanner is capable of acquiring 20,000–50,000 points on the liver surface for each acquisition. Each acquisition takes approximately 20 s, with another minute for positioning as the experimental setup is not yet optimized. In comparison, using the standard rate of 40 Hz for point acquisition with the tracked probe, it would take more than 6 min to acquire the same amount of points. The results from the registration experiments indicate that the range scanner provides a better likelihood of an accurate, robust registration than does the optically tracked pen probe. In addition, the range scanner provides uniformly sampled data using a noncontact method. Both of these features limit the amount of error in surface acquisition compared to the tracked probe. These differences are showcased in Fig. 9. As a result, the range scanner provides data for a surface registration that is independent of segmentation method as indicated in Table 2. Table 3 shows the large differences in registration results with respect to segmentation method when using the tracked probe. As semiautomatic segmentation becomes less influenced by registration, hours of user interaction time can be saved before the procedure.

While the overall number of points is important to the performance of the registration, so is the information that they contain. If the range scanner captures a region that is relatively planar, then the ICP algorithm could determine multiple alignments that provide equally suitable matches. As a result, a misalignment could be determined to be equally as desirable as the correct registration. However, when geometrically unique regions of the liver are captured, many of the false matches are eliminated. The most practical feature in terms of exposure is the inferior edge of the liver near the junction of the left and right lobes at segments III, IV, and V. In case 7, there was very little information about the ridge present in the range scan, which causes a visible misalignment (shown in Fig. 11). In this figure, the notch where the falciform ligament usually resides serves as a qualitative landmark. The misalignment causes this landmark to rotate clockwise as indicated by the arrows. Also, Table 2 indicates that case 7 has the highest difference in registration between the two segmentation methods among the cases with range scan data. This is another indicator that relatively planar surfaces do not

**Table 5** Approximate Time Requirements for the Tasks in Image-guided Liver Surgery

Task	Approximate time
Preoperative tasks	
Manual segmentation	3–4 h
Automatic segmentation	15 min
Marching cubes	5 min
Radial basis function Surface Fitting	5 min
Range scan calibration	5 min
Intraoperative tasks	
Landmark localization and registration*	30 s
Surface acquisition with tracked probe*	1–2 min
Range scan setup (not optimized)	1–2 min
Surface acquisition with range scanner*	15–20 s
ICP registration using <i>k-d</i> trees	1–5 min
Modeling with finite element method	2–3 min
Image deformation	2–3 min

\*These tasks need to be performed during an apneic period.

produce a unique alignment and are susceptible to misregistration. To confirm the assertion that the ridge produces robust surface registrations, multiple registrations were performed on the same data while perturbing the initial alignment. The registration converged to the correct alignment over a higher range of perturbations when a pronounced ridge was present. As a result, the range scanner is now oriented at more of an angle rather than an overhead perspective of the operating field, and in some cases, the liver is repositioned to make the ridge more accessible. This increases the likelihood that unique surface features are acquired from the liver.

In all cases, a significant component of the rigid registration error can be attributed to nonrigid deformation. The intraoperative forces and manipulation cause noticeable shape changes in the liver compared to the preoperative images. When deformation is encountered by the rigid ICP registration, it interprets this nonrigid motion as a registration error. In some cases, such as case 7, the change in shape may be one of the factors inducing a misalignment. In each of the four cases displayed in Fig. 10, there is strong agreement between the intraoperative data and the preoperative image surface after being deformed by the finite element model. This outcome is the direct result of the boundary conditions explicitly driving the boundary nodes to the intraoperative data. Because only an incomplete region of the liver surface is acquired during surgery, boundary conditions from these areas must recover most of the intraoperative deformations. The finite element model is desirable for this application because it determines a deformation that is based on the underlying biomechanics. In phantom studies, the FEM was able to recover deformations on the order of 3–4 cm to within a subsurface target error of 4.0 mm.<sup>56</sup> Currently, the finite element studies are conducted retrospectively, and future studies will determine the logistics of incorporating the required computational resources into the operating-room system.

While accuracy for image-guided systems is paramount, the amount of time required by this technology also plays a role in feasibility. Increased time under anesthesia could provide a health risk to the patient. In our framework, most of the time-consuming tasks are part of the preoperative preparation and often take place several days before the procedure. None of the intraoperative tasks takes more than a few minutes, and only surface acquisition and registration evaluation require apneic periods. Because all apneic periods are initiated at the same point of the respiratory cycle, a single surface registration should hold over many apneic periods. Major events, such as readjustment of the liver or resection, may require another registration. A summary of the events in IGS along with the time required to perform each task is located in Table 5.

## Conclusions

We present some initial data regarding intraoperative surface registration for open abdominal hepatic tumor resection procedures. Respiration motion has been quantified as one-dimensional and periodic. This motion is primarily aligned in the cranial–caudal direction although the liver is slightly reoriented during the surgical process. Registrations were robust and accurate when using dense surface data acquired intraoperatively from the range scanner. Additionally, these registrations performed better when the range scan data were able to capture the unique geometric information from the ridges on the liver surface. Using the ridge as a target surface, the error calculated from average normal distance was less than 1 cm. Finally, finite element modeling was implemented to compensate for intraoperative deformation. It was shown to qualitatively improve the alignment by deforming the preoperative mesh to match the intraoperative conditions captured by the range scanner.

**Acknowledgments** The authors would like to acknowledge Mary Ann Laflin, a research nurse at Washington University, who was instrumental in facilitating and coordinating the clinical studies of this research. We were aided in the task of preoperative image acquisition by Dr. Bae, a professor of the Radiology Department at Washington University, as well as Tina Herron, Nita Collins, and the rest of the CT staff in Vanderbilt University's Department of Radiology. The authors would also like to thank the hepatic surgical nursing teams of Vanderbilt University and Washington University for their patience and help during the procedure. Most of the registration and visualization algorithms were developed using the Visualization ToolKit (<http://www.vtk.org>). Some segmentation and calculation were performed using the Analyze AVW Version 3.1, which was provided in collaboration with the Mayo Foundation, Rochester, Minnesota.

This work was done under the funding of NIH grant R33-CA91352.

## References

1. American Cancer Society. Cancer Facts And Figures, 2004. Available at <http://www.cancer.org>.
2. Steele GD Jr. The national cancer data base report on colorectal cancer. *Cancer* 1994;74:1979–1989.
3. Bengmark S, Hafstrom L. The natural history of primary and secondary malignant tumors of the liver. I. The prognosis for patients with hepatic metastases from colonic and rectal carcinoma by laparotomy. *Cancer* 1969;23:198–202.
4. Wood CB, Gillis CR, Blumgart LH. A retrospective study of the natural history of patients with liver metastases from colorectal cancer. *Clin Oncol* 1976;2:285–288.
5. Zavadsky KE, Lee YT. Liver metastases from colorectal–carcinoma—incidence, resectability, and survival results. *Am Surg* 1994;60:929–933.
6. Stangl R, Altendorf-Hofmann A, Charnley RM, Scheele J. Factors influencing the natural history of colorectal liver metastases. *Lancet* 1994;343:1405–1410.
7. Sardi A, Akbarov A, Conaway G. Management of primary and metastatic tumors to the liver. *Oncology (Williston Park)* 1996;10:911–925.

8. Ruers T, Bleichrodt RP. Treatment of liver metastases, an update on the possibilities and results. *Eur J Cancer* 2002;38:1023–1033.
9. Moroz P, Salama PR, Gray BN. Resecting large numbers of hepatic colorectal metastases. *ANZ J Surg* 2002;72:5–10.
10. Leow CK, Lau WY, Li AK. Surgical resection of colorectal hepatic metastases. *Hong Kong Med J* 1997;3:50–56.
11. Sotsky TK, Ravikumar TS. Cryotherapy in the treatment of liver metastases from colorectal cancer. *Semin Oncol* 2002;29:183–191.
12. Huang A, McCall JM, Weston MD, Mathur P, Quinn H, Henderson DC, Allen-Mersh TG. Phase I study of percutaneous cryotherapy for colorectal liver metastasis. *Br J Surg* 2002;89:303–310.
13. Parikh AA, Curley SA, Fornage BD, Ellis LM. Radiofrequency ablation of hepatic metastases. *Semin Oncol* 2002;29:168–182.
14. Dick EA, Taylor-Robinson SD, Thomas HC, Gedroyc WM. Ablative therapy for liver tumours. *Gut* 2002;50:733–739.
15. Wong SL, Edwards MJ, Chao C, Simpson D, McMasters KM. Radiofrequency ablation for unresectable hepatic tumors. *Am J Surg* 2001;182:552–557.
16. Clifford MA, Banovac F, Levy E, Cleary K. Assessment of hepatic motion secondary to respiration for computer assisted interventions. *Comput Aided Surg* 2002;7:291–299.
17. Rohlfsing T, Maurer CR, O'Dell WG, Zhong JH. Modeling liver motion and deformation during the respiratory cycle using intensity-based nonrigid registration of gated MR images. *Med Phys* 2004;31:427–432.
18. Shimizu S, Shirato B, Xo B, Kagei K, Nishioka T, Hashimoto S, Tsuchiya K, Aoyama H, Miyasaka K. Three-dimensional movement of a liver tumor detected by high-speed magnetic resonance imaging. *Radiother Oncol* 1999;50:367–370.
19. Korin HW, Ehman RL, Riederer SJ, Felmler JP, Grimm RC. Respiratory kinematics of the upper abdominal organs: a quantitative study. *Magn Reson Med* 1992;23:172–178.
20. Suramo I, Paivansalo M, Myllyla V. Cranio-caudal movements of the liver, pancreas and kidneys in respiration. *Acta Radiol Diagn* 1984;25:129–131.
21. Herline AJ, Stefansic JD, Debelak JP, Hartmann SL, Pinson CW, Galloway RL, Chapman WC. Image-guided surgery: preliminary feasibility studies of frameless stereotactic liver surgery. *Arch Surg* 1999;134:644–649.
22. Banovac F, Glossop N, Lindisch D, Tanaka D, Levy E, Cleary K. Liver tumor biopsy in a respiring phantom with the assistance of a novel electromagnetic navigation device. In: *Medical Image Computing and Computer-Assisted Intervention—MICCAI 2002. Lecture Notes in Computer Science*, vol. 2488. Heidelberg: Springer-Verlag, 2002, pp 200–207.
23. Herline AJ, Herring JL, Stefansic JD, Chapman WC, Galloway RL, Dawant BM. Surface registration for use in interactive image-guided liver surgery. In: *Medical Image Computing and Computer-Assisted Intervention—MICCAI 1999. Lecture Notes in Computer Science*, vol. 1679. Heidelberg: Springer-Verlag, 1999, pp 892–899.
24. Voirin D, Payana Y, Amavizca M, Létoublon C, Troccha J. Computer-aided hepatic tumour ablation: requirements and preliminary results. *C R Biol* 2002;325:309–319.
25. Furushiro N, Saito T, Masutani Y, Sakuma I. Specification method of surface measurement for surgical navigation: ridgeline based organ registration. *Lecture Notes in Computer Science*, vol. 2489. Heidelberg: Springer-Verlag, 2002, pp 109–115.
26. Cash DM, Sinha TK, Chapman WC, Terawaki H, Dawant BM, Galloway RL, Miga MI. Incorporation of a laser range scanner into image-guided liver surgery: surface acquisition, registration, and tracking. *Med Phys* 2003;30:1671–1682.
27. Aylward SR, Jomier J, Guyon JP, Weeks S. Intra-operative 3D ultrasound augmentation. In: *2002 IEEE International Symposium on Biomedical Imaging*. 2002, pp 421–424.
28. Porter BC, Rubens DJ, Strang JG, Smith J, Totterman S, Parker KJ. Three-dimensional registration and fusion of ultrasound and MRI using major vessels as fiducial markers. *IEEE Trans Med Imag* 2001;20:354–359.
29. Hassenpflug P, Schobinger M, Vetter M, Ludwig R, Wolf I, Thorn M, Grenacher L, Richter GM, Uhl W, Buchler MW, Meinzer HP. Generation of attributed relational vessel graphs from three-dimensional freehand ultrasound for intraoperative registration in image-guided liver surgery. In *Galloway RL, ed. Medical Imaging 2003—Visualization, Image-Guided Procedures, and Display*. Proceedings of SPIE, vol. 5029, 2003, pp 222–230.
30. Penney GP, Blackall JM, Hamady MS, Sabharwal T, Adam A, Hawkes D. Registration of freehand 3D ultrasound and magnetic resonance liver images. *Med Image Anal* 2004;8:81–91.
31. Carrillo A, Duerk JL, Lewin JS, Wilson DL. Semiautomatic 3-D image registration as applied to interventional MRI liver cancer treatment. *IEEE Trans Med Imag* 2000;19:175–185.
32. Wilson DL, Carrillo A, Zheng L, Genc A, Duerk JL, Lewin JS. Evaluation of 3D image registration as applied to MR-guided thermal treatment of liver cancer. *J Magn Reson Imaging* 1998;8:77–84.
33. Cao Z, Pan S, Li R, Balachandran R, Fitzpatrick JM, Chapman WC, Dawant BM. Registration of medical images using an interpolated closest point transform: method and validation. *Med Image Anal* 2004;8:421–427.
34. Hermoye L, Laamari-Azjal I, Cao Z, Annet L, Lerut J, Dawant BM, Van Beers BE. Liver segmentation in living liver transplant donors: comparison of semiautomatic and manual methods. *Radiology* 2005;234:171–178.
35. Malladi R, Sethian JA, Vemuri BC. Shape modeling with front propagation: a level set approach. *IEEE Trans Pattern Anal Mach Intell* 1995;17:158–175.
36. Lorensen WE, Cline HE. Marching cubes: a high resolution 3D surface construction algorithm. *ACM Comput Graph* 1987;21:163–169.
37. Carr JC, Beatson RK, McCallum BC, Fright WR, McLennan TJ, Mitchell TJ. Smooth surface reconstruction from noisy range data. In: *ACM GRAPHITE 2003*. Melbourne, Australia, 2003, pp 119–126.
38. Northern Digital Inc. OPTOTRAK—Technical Specifications, 2002. [http://www.ndigital.com/optotrak\\_technical.html](http://www.ndigital.com/optotrak_technical.html).
39. Kynor DB, Friets EM, Knaus DA, Bieszczad J. Tissue localization using endoscopic laser projection for image-guided surgery. In *Galloway RL, Cleary KR, eds. Medical Imaging 2005: Visualization, Image-Guided Procedures*. Proceedings of SPIE, vol. 5744, 2005, pp 225–235.
40. Cash DM, Sinha TK, Galloway RL, Chapman WC, Terawaki H, Miga MI. Incorporation of a laser range scanner into an image-guided surgical system. In *Galloway RL, ed. Medical Imaging 2003: Visualization, Display, and Image-guided Procedures*. Proceedings of SPIE, vol. 5029, 2003, pp 269–280.
41. Sinha TK, Dawant BM, Duay V, Cash DM, Weil RJ, Miga MI. A method to track cortical surface deformations using a laser range scanner. *IEEE Trans Med Imag* 2005;24:767–781.
42. Besl PJ, McKay ND. A method for registration of 3-D shapes. *IEEE Trans Pattern Anal Mach Intell* 1992;14:239–256.
43. Bentley JL. Multidimensional binary search trees used for associative searching. *Commun ACM* 1975;18:509–517.
44. Zhang ZY. Iterative point matching for registration of free-form curves and surfaces. *Int J Comput Vis* 1994;13:119–152.
45. Horn BKP. Closed-form solution of absolute orientation using unit quaternions. *J Opt Soc Am* 1987;4:629–642.
46. Schonemann PH. A generalized solution of the orthogonal procrustes problem. *Psychometrika* 1966;31:1–10.
47. Arun KS, Huang TS, Blostein SD. Least-squares fitting of 2 3-D point sets. *IEEE Trans Pattern Anal Mach Intell* 1987;9:699–700.
48. Miga MI, Paulsen KD, Lemery JM, Eisner SD, Hartov A, Kennedy FE, Roberts DW. Model-updated image guidance: initial

- clinical experiences with gravity-induced brain deformation. *IEEE Trans Med Imag* 1999;18:866–874.
49. Roberts DW, Miga MI, Hartov A, Eisner S, Lemery JM, Kennedy FE, Paulsen KD. Intraoperatively updated neuroimaging using brain modeling and sparse data. *Neurosurgery* 1999;45:1199–1206.
  50. Skrinjar O, Nabavi A, Duncan J. Model-driven brain shift compensation. *Med Image Anal* 2002;6:361–373.
  51. Ferrant M, Nabavi A, Macq B, Jolesz FA, Kikinis R, Warfield SK. Registration of 3-D intraoperative MR images of the brain using a finite-element biomechanical model. *IEEE Trans Med Imag* 2001;20:1384–1397.
  52. Marescaux J, Clement JM, Tasseti V, Koehl C, Cotin S, Russier Y, Mutter D, Delingette H, Ayache N. Virtual reality applied to hepatic surgery simulation: the next revolution. *Ann Surg* 1998;228:627–634.
  53. Cotin S, Delingette H, Ayache N. Real-time elastic deformations of soft tissues for surgery simulation. *IEEE Trans Vis Comput Graph* 1999;5:62–73.
  54. Szekely G, Brechbuhler C, Hutter R, Rhomberg A, Ironmonger N, Schmid P. Modelling of soft tissue deformation for laparoscopic surgery simulation. *Med Image Anal* 2000;4:57–66.
  55. Soler L, Delingette H, Malandain G, Ayache N, Koehl C, Clement JM, Dourthe O, Marescaux J. An automatic virtual patient reconstruction from CT-scans for hepatic surgical planning. *Stud Health Technol Inform* 2000;70:316–322.
  56. Cash DM, Sinha TK, Chapman WC, Galloway RL, Miga MI. Compensating for intraoperative soft tissue deformations using incomplete surface data and finite elements. *IEEE Trans Med Imag* 2005;24:1479–1491.
  57. Preim B, Selle D, Spindler W, Oldhafer KJ, Peitgen HO. Interaction techniques and vessel analysis for preoperative planning in liver surgery. In: *Medical Image Computing and Computer-Assisted Intervention—MICCAI 2000. Lecture Notes in Computer Science*, vol. 1935. Heidelberg: Springer-Verlag, 2000, pp 608–617.
  58. Miga MI, Cash DM, Cao Z, Galloway RL, Dawant B, Chapman WC. Intraoperative registration of the liver for image-guided surgery using laser range scanning and deformable models. In Galloway RL, ed. *Medical Imaging 2003: Visualization, Image-Guided Procedures, and Display. Proceedings of SPIE*, vol. 5029, 2003, pp 350–359.